surfaces

MDPI

Article

Mapping Acid–Base Sites on Anatase Titania (100) and (101) Surfaces by Density Functional Theory: The Link Between Lewis Acidity and the Surface Ability to Flex

Alexey V. Ignatchenko * and Paige E. Denman

Chemistry Department, St. John Fisher University, 3690 East Avenue, Rochester, NY 14618, USA; ped09843@sjfc.edu

* Correspondence: aignatchenko@sjfc.edu or alexey.ignatchenko@gmail.com; Tel.: +1-(585)-385-8385

Abstract: The acidity of anatase titania before and after KOH doping was probed by pyridine adsorption in a pulse microreactor and modeled by DFT optimization of the geometry of CO and pyridine adsorption on a periodic slab of (101) and (100) surfaces using a GGA/PBE functional and verified by an example of a single-point calculation of the optimized geometry using an HSE-06 hybrid functional. The anatase (101) surface was slightly more acidic compared to the (100) surface. Both experimental and computational methods show that the acidity of anatase surfaces decreased after KOH doping and increased after the dissociative adsorption of water. Higher acidity of Ti metal centers was indicated by the shortening of the Ti-N, Ti-C, and C-O bond lengths, increasing the IR frequency of CO and pyridine ring vibrations and energy of adsorption. The DFT calculated energy of pyridine adsorption was analyzed in terms of binding energy and the energy of lattice distortion. The latter was used to construct Hammett plots for the adsorption of 4-substituted pyridines with electron-donating and -withdrawing substituents. The Hammett rho constant was obtained and used to characterize the acidity of various metal centers of −1.51 vs. −1.46 on pristine (101) and (100) surfaces, which were lowered to −1.07 and −1.19 values on KOH-doped (101) and (100) surfaces, respectively. The mechanism of lowering surface acidity via KOH doping proceeds through the stabilization of the atomic structure of Lewis acid centers. When an alkaline metal cation binds to several lattice oxygen atoms, the surface structure becomes more rigid. The ability of Ti atoms to move toward the adsorbate is restricted. Consequently, the lattice distortion energy and binding energy are decreased. In contrast, higher flexibility of the outermost layer of Ti atoms as a result of electron density redistribution, for example, in the presence of water on the surface, allows them to move farther outward, make shorter contacts with the adsorbate, and attain higher energies of binding and lattice distortion.

Keywords: surface acidity; anatase titania; adsorption; DFT calculation; lateral interaction; Hammett plot

Citation: Ignatchenko, A.V.; Denman, P.E. Mapping Acid–Base Sites on Anatase Titania (100) and (101) Surfaces by Density Functional Theory: The Link Between Lewis Acidity and the Surface Ability to Flex. *Surfaces* **2024**, *7*, 1060–1078. https://doi.org/10.3390/surfaces7040070

Academic Editors: Jaeho Kim and Susumu Yonezawa

Received: 12 November 2024
Revised: 12 December 2024
Accepted: 16 December 2024
Published: 19 December 2024

1. Introduction

The deposition of alkali metals is a key method for modifying surface acid–base properties. Alkaline doping of metal oxides significantly improves their catalytic activity and catalyst stability for several catalytic processes involving renewable energy and fuel production. Examples include titanium oxide photocatalytic oxidation of organic materials and photolysis of water [1], dehydration of methanol to dimethyl ether [2], and decarboxylative ketonization (preparation of ketones from carboxylic acids proceeding with decarboxylation) [3–6], an important step in biofuel upgrading [7]. Alkaline doping produces a remarkably contrasting effect between metal oxide catalysts, such as monoclinic zirconia and anatase titania, not seen for other TiO_2 polymorphs, such as brookite and rutile, with an unprecedented selectivity switch from the symmetrical to the cross-product in the preparation of methyl ketones [8,9], an important class of industrial intermediates, which is attainable in biorefineries [10]. The reason for the doping action is only partially

understood [9,11] but is undeniably dependent on the synergistic role of acid–base pairs within the catalytic sites [12,13]. Acid–base pairs play a definite role in the decarboxylative ketonization mechanism, which starts from the mainly dissociative adsorption of carboxylic acids on metal oxides generating protons as a highly mobile acid attached to the lattice oxygen atoms and the less mobile carboxylate acting as a base bound to the acidic metal centers [14–17].

To elucidate the above catalytic mechanisms, we decided to study the dependence of the acidity–basicity function of well-defined anatase titania surfaces on adsorbate coverage and the degree of alkaline doping. Such knowledge could help us to explain the specific response of anatase catalysts to the presence of alkaline metals. The initial target was an idealized surface free from defects or adsorbate reactions by the classic approach of probing molecule adsorption. Upon close examination, a new physical phenomenon was discovered by DFT methods during the surface response to the probing process while revealing the role of alkaline metal promoters in surface stabilization.

Although acidity and basicity are fundamental concepts in chemistry for characterizing reactivity in the gas phase or in solution, they are difficult to quantify when applied to surfaces. The acid and base properties of molecules are well understood in terms of Lewis or Bronsted theories and quantitatively measured through the equilibrium constant involving a conjugate pair of acid and base, for example, through the pKa values in solution. Conversely, the characterization of solid surfaces is more complicated due to the variety of atomically scaled groups with a broad range of acid–base strengths [18]. The acid–base equilibrium on the gas–solid interface involves a range of individual surface centers. Unlike in solution, their acid–base strength is not mediated by the presence of a solvent enabling proton exchanges. Instead, the equilibrium at each center is affected by the events taking place nearby on the surface through the mechanism of altering the surface structure. The adsorption of probe molecules on metal oxide surfaces with different oxidation states of metal cations and local geometries—different facets or edges, corners, steps, and kinks—is believed to be the reason for the observation of a broad range of surface acidities. Yet, the classification of acid centers as weak, medium, or strong is often used, for example, by the Temperature Programmed Desorption (TPD) method, which is too broad and not well-defined [19]. A major drawback of TPD is its operation under nonequilibrium conditions, thus lacking the essential requirement for comparative measurements. Also, it can be misleading because the lateral effects of adsorbates bound on sites with equal acidity may create an appearance of surface heterogeneity in TPD analysis, not owing to local geometry or oxidation state differences. Differentiation between weak and strong acidity in TPD analysis may arise as an artifact. At high coverage and low temperatures, adsorbates are loosely bound, suggesting weak acidity. As the temperature rises and coverage drops, stronger binding at the remaining sites indicates stronger acidity. Due to the above limitations of TPD, vibrational spectroscopy [20] is a more common method to study surface acidity, which offers the advantage of maintaining equilibrium at any desired constant temperature. Both weakly and strongly binding probing molecules are used. Typical examples include CO, NO, CO_2, ammonia, pyridine, or tetrahydrofuran molecules that can change the frequency of certain vibrations affecting the basic center of the probing molecule and the acidic center on the surface proportionally to the energy of the acid–base interaction [20,21]. However, the spectroscopy method also measures acidity, which still depends on coverage. To overcome the problem of weakening adsorption energy per molecule at increasing coverage, it has been suggested to restrict the analysis to a minimum coverage and use probing molecules showing minimal interaction energy, therefore causing the smallest perturbation of the surface structure [18]. Such an approach may not accurately reflect catalytic processes under high surface coverage by moderate or strong binding adsorbates. To overcome the above problems, we decided to study and compare the application of weak and strong basic probe molecules and justify the possible use of the latter.

Another problem is steric repulsion, which is believed to be responsible for adsorbate–adsorbate interactions that reduce the binding energy of neighboring adsorbates. Participation of the surface lattice in producing this effect is acknowledged but not sufficiently understood [22,23]; therefore, it is interesting to explore. In addition, it is of interest to see if the adsorption energy is closely related to surface polarizability as it has been proposed in the form of a general concept [24].

Finally, we would like to justify our choice of computational method. Recently, the use of computationally expensive hybrid functionals, such as HSE [25] or the DFT+U approach [26], to better handle electronic correlation effects has been recommended in numerous studies on electronic structures and adsorption on anatase titania dedicated to its photocatalytic properties [27] at the expense of increasing CPU time by up to one or two orders of magnitude. It has been suggested that the less expensive GGA method does not accurately capture the localized d-states of reducible atoms, such as titanium, leading to underestimated band gaps that are important in photocatalysis. Also, PBE's tendency to over-delocalize electrons can lead to weaker adsorption energies for adsorbates that interact strongly with the surface and likely reduce the local Ti charge on the adsorption site from +4 to +3. However, the enormous task of mapping major anatase titania surfaces by screening a vast number of adsorption states with a broad range of adsorbates of different basicities with six choices and coverages with up to four choices and then comparing the same set under the influence of alkaline metal dopants and water presence on the calculated Lewis acidity is simply unattainable with hybrid functionals. The total number of computational runs with full geometry optimization exceeded a hundred and twenty. Use of a computationally cheap DFT method by the generalized gradient approximation (GGA) approach with the Perdew–Burke–Ernzerhof (PBE) exchange–correlation functional is the only practical option, which takes an average CPU time between 24 and 220 h per run with 24–64 parallel processors. To make the right choice, we tested and compared the results of pyridine binding energy with PBE vs. a hybrid HSE-06 functional in one specific case and found only an insignificant difference. Even if the bulk of the calculations performed with the PBE functional still have a small systematic error for each calculated point, there is no reason to believe that the direction of the overall trend for the adsorption energies' dependence on the variation of sites and the basicity of the substituted pyridines can be overturned. Therefore, all computations were performed using the GGA/PBE method.

2. Experimental Section and Computational Methods

Instruments: GC/MS data were obtained using a TRACE1300 gas chromatograph manufactured by Thermo Fisher Scientific, Inc., Waltham, MA, USA, equipped with a Thermo Scientific ISQ Single Quadrupole mass selective detector and HP-5 MS UI capillary column, 30 m in length, 0.25 mm in diameter, and 0.25 mkm phase thickness.

Anatase sample preparation: Commercial anatase TiO_2 pellets obtained from Alfa Aesar, Haverhill, MA, USA, with a BET surface area of 37 m^2/g and pore volume of 0.29 mL/g were crushed and sieved to obtain a fraction with a particle size less than 0.25 mm. Doping by KOH was performed according to the literature procedure as follows [28]: Commercial anatase pellets (100 g) were soaked in 100 mL of 10% by-weight KOH solution in water for 24 h at 60 °C under reduced pressure. After soaking, the KOH solution was drained, and the sample was washed three times with 100 mL of deionized water. It was dried at 130 °C for 4 h, followed by calcination at 450 °C for 2 h with a heating rate of 1 °C/min. The pellets were subsequently crushed and sieved, and the fraction with a particle size of less than 0.25 mm and a BET surface area of 42 m^2/g was collected for adsorption studies.

Pyridine adsorption study: A sample with and without the KOH dopant in a 5–20 mg portion was loaded into the "inside-GC" pulse microreactor [29,30] and saturated with vapors of pyridine in helium carrier gas by injecting ten pulses of 1.0 µL at temperatures ranging from 200 to 350 °C. Twenty pulses of 0.1 µL of water were added within 100–200 min, and the integral amount of pyridine displaced by water from the surface to the gas phase was measured by GC/MS monitoring at m/z 18 for water and m/z 79 for pyridine. The typical titration curves are shown in Figure S15. Calibration was performed by GC/MS analysis

using an equimolar mixture of pyridine and water in the absence of the anatase sample at temperatures ranging from 200 to 350 °C (Figure S16). The coverage was calculated using the sample weight, BET area, and the average concentration of Ti sites of 5.7 nm^{-2} on anatase titania as determined by DFT studies [30,31].

The DFT computational package $DMOL^3$ supplied by Dassault Systèmes Biovia Corporation [32,33] was used to construct a periodic slab of anatase titania (100) and (101) stoichiometric surfaces. The crystal structure was built based on bulk lattice parameters published for anatase titania [34] and adjusted by computing and minimizing its energy. The unit cell had a depth of six layers containing 16 coordinatively unsaturated Ti and 32 oxygen atoms in each layer for a total of 96 TiO_2 molecules. The coordinates of the two bottom layers were constrained to represent the bulk crystal, while the top four layers were allowed to relax. The topmost layer had 16 mono-coordinatively unsaturated Ti atoms. The surface geometry optimization of the periodic slab was performed within GGA for the electron–electron interaction based on the work of Perdew et al. using the PBE functional [35] with the double numerical plus polarization basis set until SCF density convergence, optimization energy convergence, and gradient convergence achieved 0.00001, 0.00002, and 0.004 a.u., respectively. The Tkatchenko–Scheffler exchange–correlation was applied to address intermolecular dispersive interactions [36]. Core electrons were treated with the all-electron relativistic option, and all calculations were spin-restricted. The real-space global orbital cutoff radius of 4.6 Å was applied. The Monkhorst–Pack parameters were derived to give 0.07 1/Å separation between neighboring grid points for integration over the Brillouin zone.

To ensure the absence of interaction between the adsorbed molecules and the next layer, a vacuum slab with a thickness of 20 Å was constructed above the surface. This thickness was deemed sufficient by comparing the total energy and bond lengths of adsorbed pyridine at vacuum thickness values of 10, 15, and 20 Å until the changes became negligible.

Harmonic vibrational frequencies were obtained from the Hessian matrix of the Cartesian second derivatives of a fully optimized relaxed surface with an adsorbate, either a CO or pyridine molecule, adsorbed on a Ti atom. The infrared intensities were calculated using the atomic polar tensors (Born effective charges) of all atoms in the unit cell, derived as the second derivative of the total energy with respect to the Cartesian coordinates and dipole moments.

For comparison purposes, a single-point energy calculation was also performed in one case of pyridine adsorption on the (100) anatase surface covered by KOH at 13% coverage using the CASTEP package [37] with the hybrid HSE-06 functional [38] and MBD dispersion correction [39] on the geometry previously optimized by GGA/PBE. Calculations were conducted with spin restriction and incorporated relativistic effects using the Koelling–Harmon scalar approach for pseudopotential generation. A plane-wave energy cutoff of 600 eV was applied, and SCF convergence and the energy change were set at 2×10^{-6} eV/atom.

3. Results

3.1. DFT Computational Study of Adsorption

A large-size unit cell with 16 TiO_2 on the topmost layer was chosen to see the effect of adsorbates' concentration on the surface in increments of 6.25% (100/16). The anatase TiO_2 (100) surface is composed of alternating islands and channels. Coordinatively unsaturated (CUS) sites include fivefold coordinated Ti atoms (Ti_{5c}) located on top of islands and twofold coordinated oxygen atoms, O_{2c}, bridging Ti atoms between islands and channels. Due to the symmetry, all CUS Ti atoms on the surface are identical. A map of the TiO_2 (100) surface in Figure 1 shows sixteen numbered sites where adsorbates can be placed to study the concentration effect.

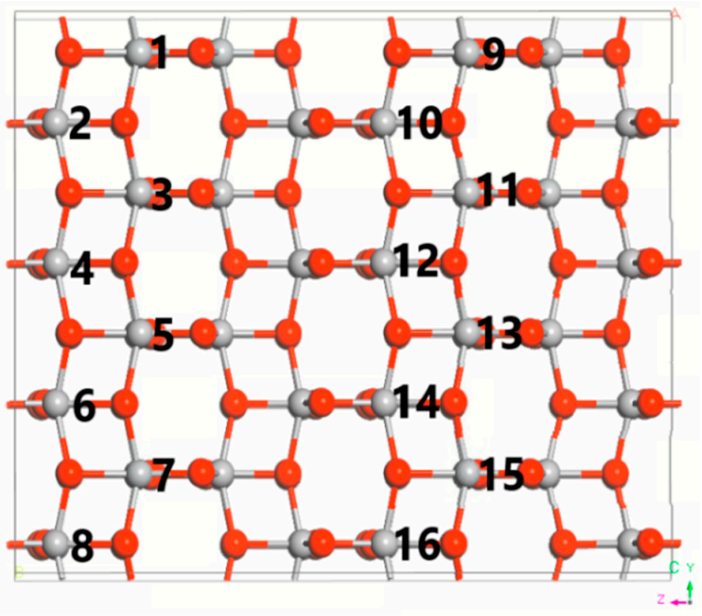

Figure 1. A map of anatase TiO_2 (100) surface showing numbered sites for Ti Lewis acid centers where adsorbates can be placed. Ti atoms are shown in light grey and oxygen in red.

Pyridine molecules adsorb on Ti_{5c} on the (100) surface, making a strong Ti-N coordination bond with the preference of orienting the ring orthogonal to the surface to maximize the interaction between the pyridine nitrogen lone pair and surface Ti Lewis acid center and avoid steric repulsion that would occur between surface oxygen atoms and aromatic π-bonds of the ring if it was parallel to the surface. The pyridine ring is oriented in the (010) plane, i.e., cross cutting islands (Figure 2), as opposed to in an orientation parallel to the islands. In addition to the Ti-N binding, there are two hydrogen bonds formed between pyridine's ortho hydrogen atoms and two types of lattice oxygen atoms O_{2c} and O_{3c} that help to stabilize the preferred adsorption configuration.

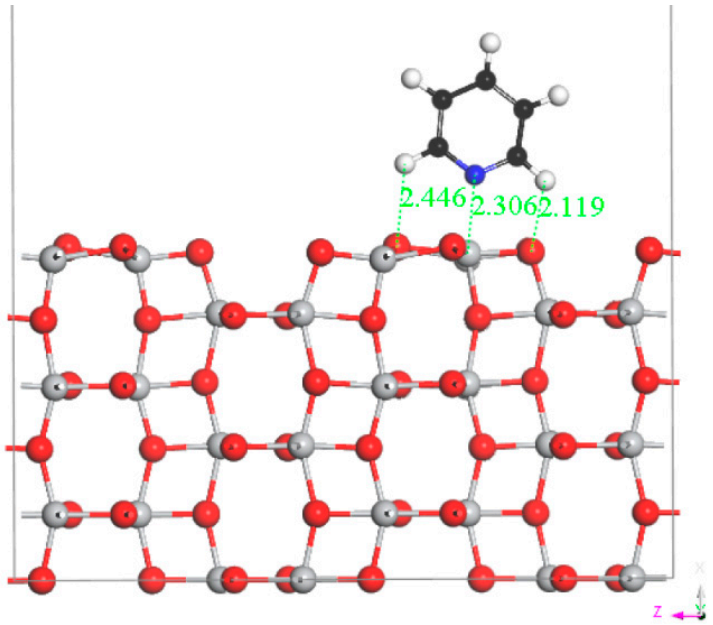

Figure 2. Preferred mode of pyridine adsorption on (100) surface of anatase TiO_2. Atom coloring is shown as follows: Ti—light grey, O—red, C—black, N—blue, and H—white. Bond distances are shown in Å.

The strength of adsorption is characterized by the energy of adsorption that is exothermic, i.e., becoming more negative, along with a shortening Ti-N bond length (Table S1). Upon adsorption, the affected Ti atom moves outward toward the adsorbate, and the surface becomes distorted compared to the relaxed pristine one. The protocol for calculating the energies of adsorption and lattice distortion is shown in Figure 3. The initial surface, either pristine or modified with KOH or water in two other cases, was allowed to relax through geometry optimization, and the energy F_1 was calculated for the relaxed surface. An **N** number of various 4-substituted pyridines was added to the surface after their geometry was optimized in the gas phase (energy $\mathbf{F_2}$), and the geometry of the periodic slab with **N** adsorbates was optimized (energy $\mathbf{F_3}$). The adsorption energy per adsorbate, $\mathbf{E_1}$, was calculated by Formula (1):

$$\mathbf{E_1} = (\mathbf{F_3} - \mathbf{F_1} - \mathbf{N} \times \mathbf{F_2})/\mathbf{N} \quad (1)$$

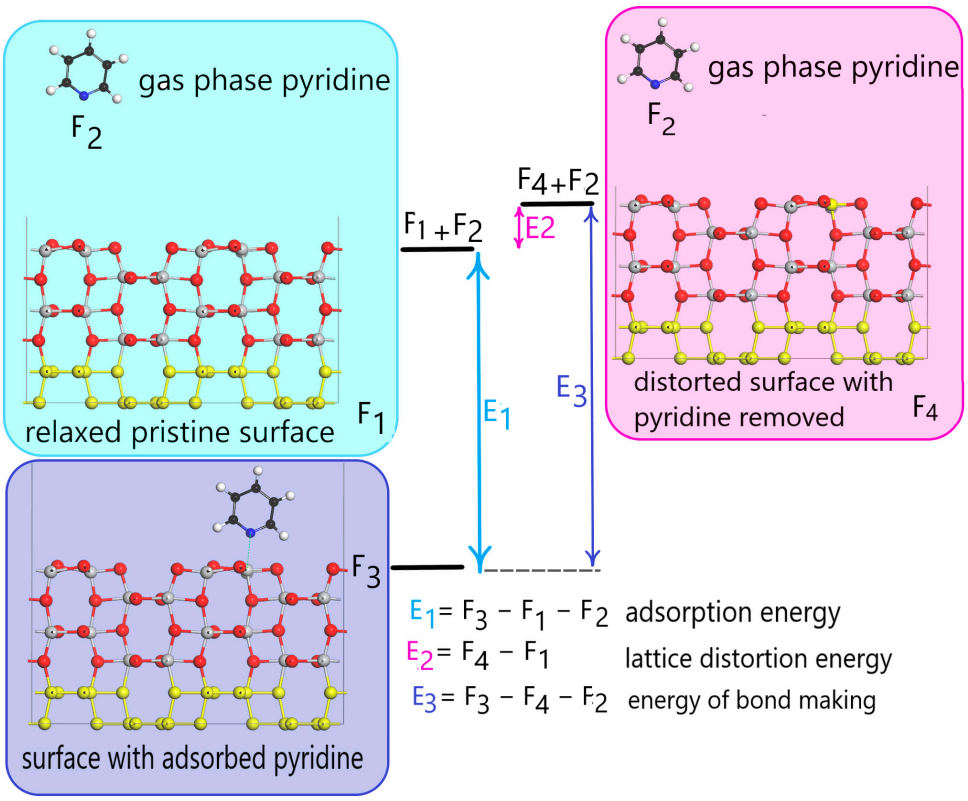

Figure 3. Calculation of energy of adsorption $\mathbf{E_1}$, lattice distortion $\mathbf{E_2}$, and the adjusted energy of adsorption $\mathbf{E_3}$. Atoms are colored as follows: Ti—light gray, O—red, C—black, N—blue, H—white, constrained Ti and O atoms representing bulk positions of the two bottom layers—yellow, and single top Ti used to host pyridine—yellow.

The adsorbates were removed, and the single-point energy for the distorted surface, $\mathbf{F_4}$, was calculated. The lattice distortion energy per one adsorbate $\mathbf{E_2}$ was calculated by Formula (2). The adjusted adsorption energy per adsorbate $\mathbf{E_3}$, which reflects the bond formation between the adsorbate and Ti atom, was calculated using Formula (3).

$$\mathbf{E_2} = (\mathbf{F_4} - \mathbf{F_1})/\mathbf{N} \quad (2)$$

$$\mathbf{E_3} = \mathbf{E_1} - \mathbf{E_2} = (\mathbf{F_3} - \mathbf{F_4} - \mathbf{N} \times \mathbf{F_2})/\mathbf{N} \quad (3)$$

For pairs of adsorbed pyridine molecules, the heat of adsorption per adsorbate becomes smaller (a less negative value) compared to that for single molecules, and it depends on the distance between the affected adsorption sites (Figure 4). The adsorption strength

sharply increases for the pair of molecules closest to each other, sites 13 and 15, on the same island. Adsorbates on those sites separated by 3.84 Å are still far enough from each other thus avoiding steric repulsion.

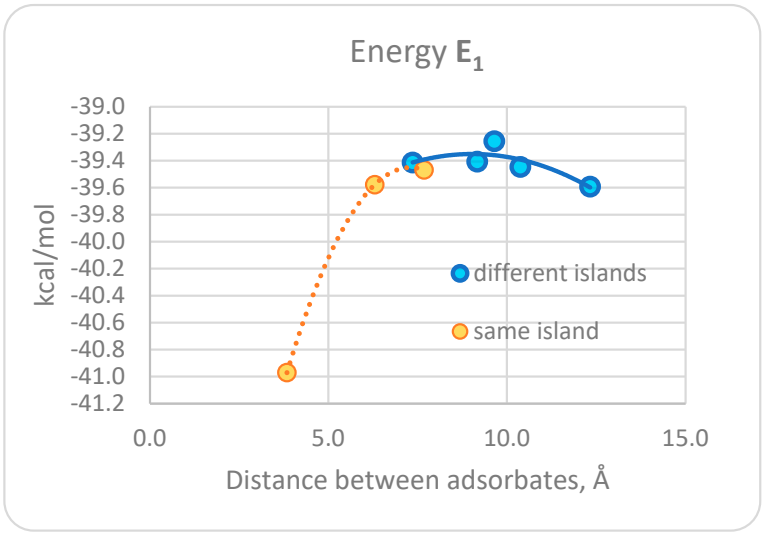

Figure 4. Energy of adsorption per adsorbate for a pair of pyridines adsorbed on sites 13–15, 12–15, and 11–15 (located on the same island, yellow dotted line) and sites 3–15, 4–15, 5–15, 6–15, and 7–15 (located on different islands, blue solid line) according to the Figure 1 map. Points on the graph from left to right appear in the order of sites listed above.

The energy $\mathbf{E_2}$ of lattice distortion caused by the adsorption of a pair of pyridine molecules (Figure 5) responds differently for adsorption on the same island vs. different ones, decreasing and increasing with the distance becoming longer, respectively.

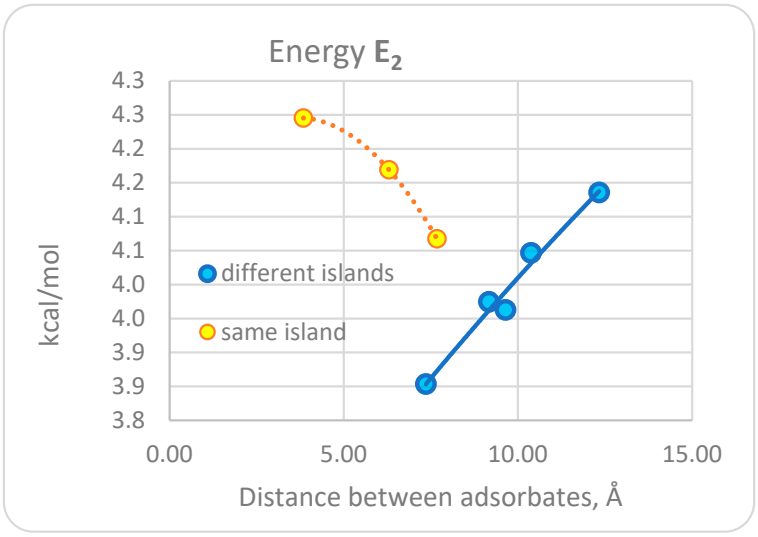

Figure 5. Lattice distortion energy, $\mathbf{E_2}$, per one adsorbate for a pair of pyridine molecules adsorbed on TiO_2 anatase (100) surface as a function of the distance between them.

The additional number of adsorbates on either island induces a proportionally increasing lattice distortion expressed as the energy per surface Ti_{5c} atom, while the value per adsorbate declines with increasing surface coverage (the blue circle graph vs. the orange diamond graph, respectively, in Figure 6), which is the expected behavior [18,23].

For the adsorption of 4-substituted pyridines, electron-donating substituents increase the basicity of the pyridine nitrogen and the binding energy, while electron-withdrawing

groups decrease it (Figure S3). Stronger adsorption causes a higher lattice distortion. The dependence of the lattice distortion energy $\mathbf{E_2}$ on the Hammett σ constant is shown in Figure 7. The substituents used and their Hammett σ constant are listed in Table S9.

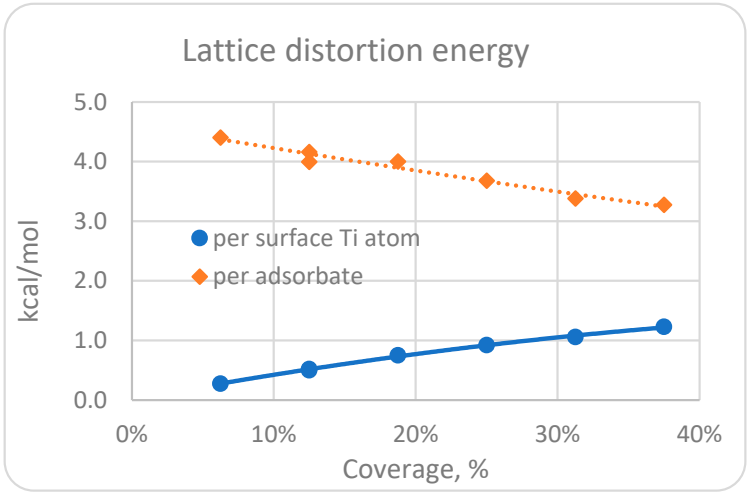

Figure 6. Lattice distortion energy expressed per surface Ti atom, blue circles, and per adsorbate, orange diamonds, upon pyridine adsorption as a function of surface coverage.

The effect of the lattice distortion energy dependence on the basicity of pyridines has been studied in the presence of water and a KOH dopant added to the (100) surface. The position of H and OH resulting from the dissociative adsorption of water was found in our previous study [30]. A map of the adsorption of pyridines in the presence of water is shown in Figure S6. The preferred position of K and OH fragments was found through geometry optimization by trial-and-error, placing K next to lattice oxygen. During geometry optimization, regardless of the initial position, potassium moves and becomes stabilized in the global energy minimum slightly above the surface in the pocket between three lattice oxygen atoms O_{2c} from the top layer and one O_{3c} from the second layer (Figure 7b and Figure S5), which allows the minimization of energy by making the maximum number of K-O bonds. Three different sites for adsorption were distinguished based on the distance to the potassium atom (Figure 7b). The single-point computation of $\mathbf{E_1}$, $\mathbf{E_2}$, and $\mathbf{E_3}$ energies for pyridine adsorption at 12.5% coverage of both KOH and pyridine on the (100) TiO_2 surface using the more accurate hybrid functional HSE06 produces energies of −32.9, 5.6, and −38.5 kcal/mol, respectively, which are not much different from those obtained with GGA/PBE at −34.6, 3.7, and −38.4 kcal/mol.

It appears that KOH presence stabilizes the lattice and lowers the distortion energy caused by pyridine adsorption, as concluded by comparing the position of the graphs with and without KOH on the energy diagram (Figure 7a). In contrast, the presence of water on the surface makes the lattice distortion energy during pyridine adsorption much higher (Figure 7c, dashed line with purple squares).

The effect of the lattice distortion during pyridine adsorption was also observed on the (101) surface. Potassium finds a place between four lattice oxygen atoms—two O_{2c} and two O_{3c}. In addition, the OH group attached to site 1 stabilizes potassium through a bond with a distance of 2.56–2.62 Å, depending on the presence of various 4-substituted pyridines (Figure 8). The adsorption of OH on site 2 is less stable by 6.9 kcal/mol per unit cell because it does not provide extra stabilization through binding to potassium (Figure S8b).

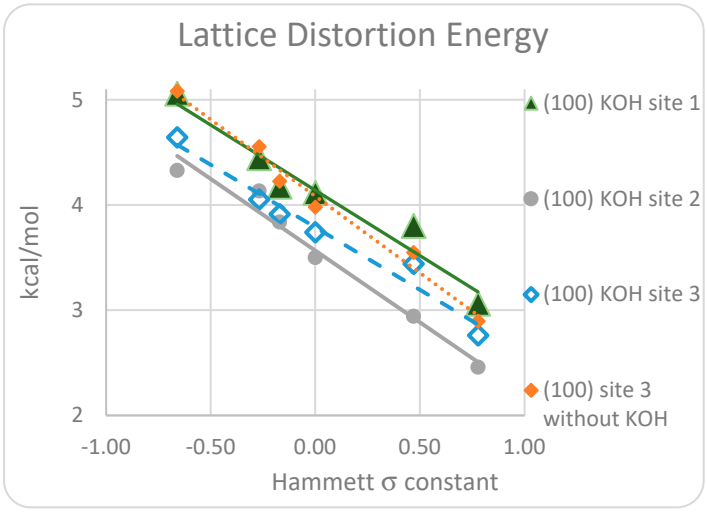

(**a**)

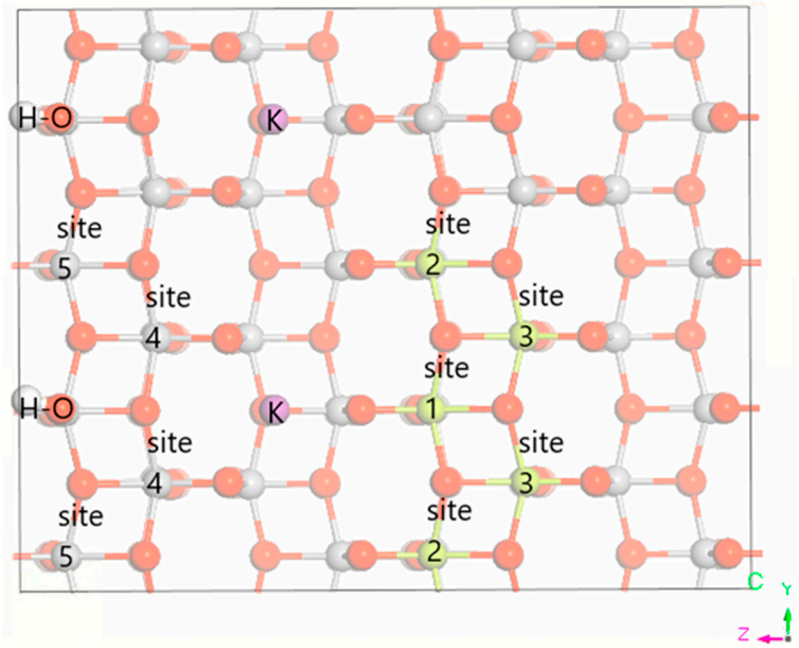

(**b**)

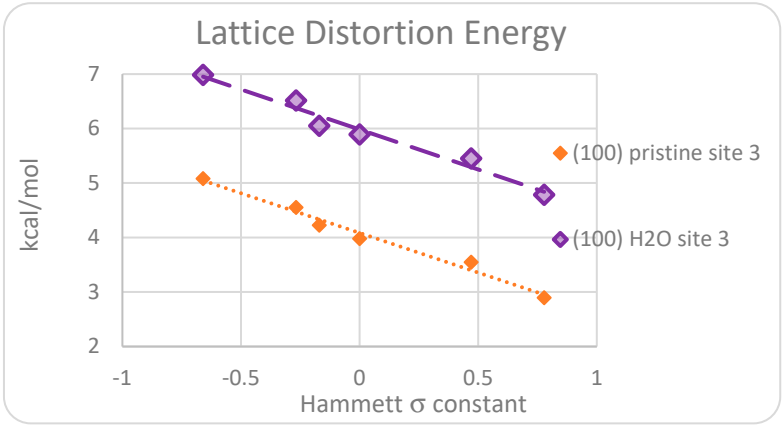

(**c**)

Figure 7. Lattice distortion energy $\mathbf{E_2}$ as a function of the Hammett σ constant for the adsorption of 4-substituted pyridines on TiO_2 anatase (100) surface (**a**) sites 1, 2, and 3 at 12.5% coverage in the absence and presence of KOH according to the (**b**) map of adsorption sites. Atoms are colored as follows: Ti—light gray and O—red. (**c**) The same on site 3 with and without presence of water.

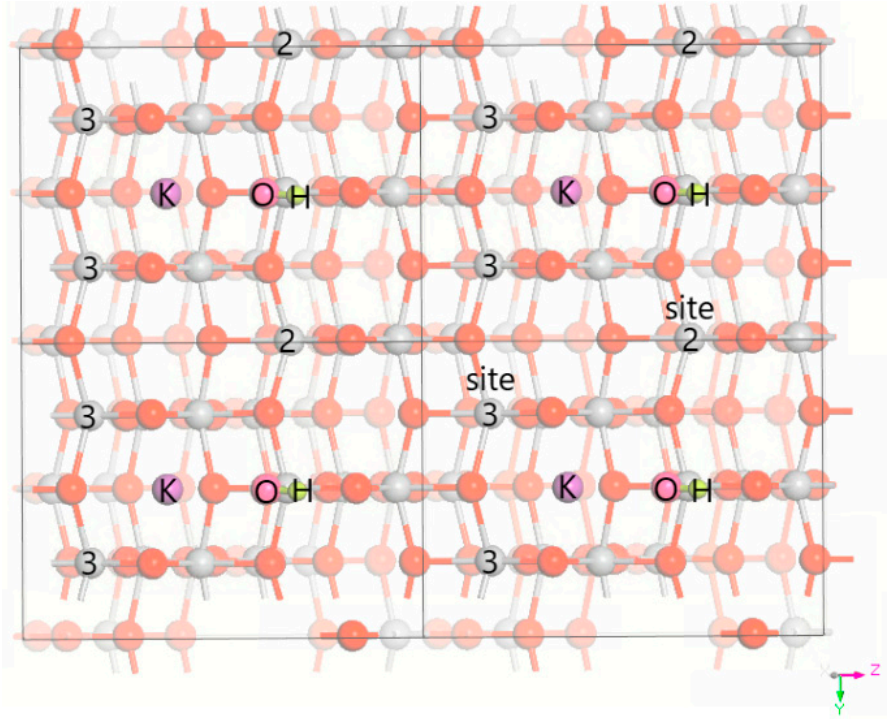

Figure 8. Map of adsorption sites for KOH-doped (101) anatase surface with OH on site 1. Atoms are colored as follows: Ti—light gray, O—red, and K—purple.

The adsorption of pyridine on sites 2 and 3 was studied for the KOH-doped anatase (101) with the OH group added on site 1 (Figures 9 and 10). In both cases, hydrogen bonding between pyridine ortho hydrogens and O_{2c} lattice atoms plays a key role in the orientation of the pyridine molecule, which is stabilized on site 2, parallel to the straight line of the top lattice atoms O_{2c}-Ti_{5c}-O_{2c} but skewed on site 3 to make a stronger H-bond with a shorter length at 1.992 vs. 2.338 Å. However, the Ti-N bond on site 2 is 0.02 Å shorter and stronger (Figure 11a), and the energy of pyridine adsorption $\mathbf{E_1}$ is 2.2 kcal/mol more exothermic compared to that on site 3 (Tables S10 and S11). The above data show that Ti CUS site 2, farther away from potassium, is more electrophilic compared to site 3.

The electrophilicity of Ti metal centers on various surfaces is characterized in Hammett plots (Figure 11b) through the dependence of the lattice distortion energy caused by pyridine adsorption, $\mathbf{E_2}$, on the Hammett constant of substituents in position 4 of pyridine. A higher value of $\mathbf{E_2}$ energy indicates a stronger electrophilic center on the surface. Energy $\mathbf{E_2}$ was chosen to obtain the electrophilicity indicator because its dependence on the Hammett σ constant is more linear, with all values of R^2 within the range of 93.3–98.1% compared to the less linear behavior for $\mathbf{E_1}$ and $\mathbf{E_3}$ energy dependence. The latter can be affected by other factors, such as hydrogen bonding. It can be seen from the graphs in Figure 11b that doping by KOH decreases the electrophilicity of Ti metal centers compared to the pristine surface and that the (101) anatase surface is more electrophilic relative to the (100) surface.

To study the effect of water presence on the (101) surface, potassium in the KOH-doped surface was replaced by H, creating several options for the position of the H attachment to nearby lattice oxygen atoms (Figure S9). The energy $\mathbf{E_1}$ of 4-substituted pyridine adsorption and lattice distortion energy $\mathbf{E_2}$ depend not only on the position of the OH group but also on the position of H (Tables S13–S15, Figure S12).

Lattice distortion energy $\mathbf{E_2}$ as a function of the Hammett σ constant was used to find the ρ constant to characterize the electrophilicity of different Ti sites on both anatase surfaces (100) and (101) (Figure 12).

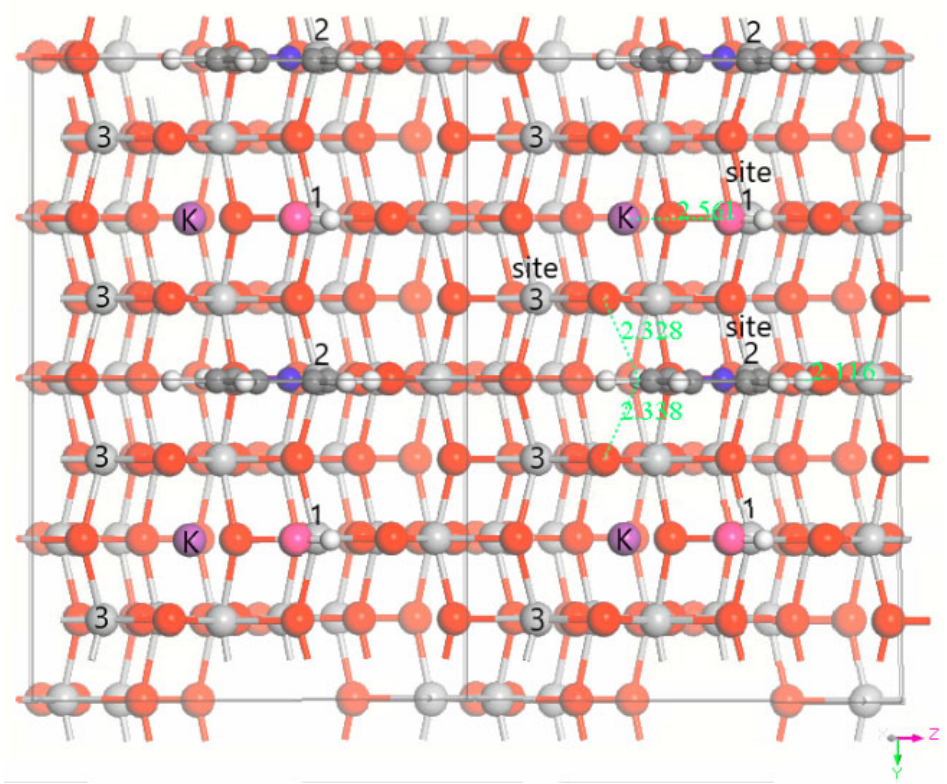

(**a**)

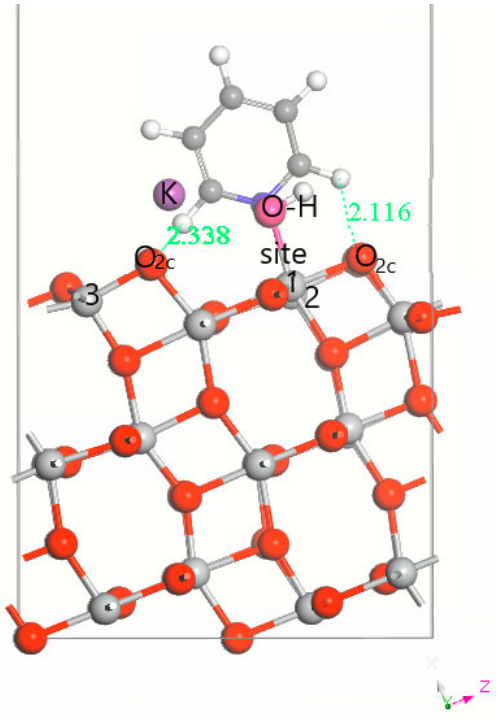

(**b**)

Figure 9. Adsorption of pyridine on site 2 with OH attached to site 1 of KOH-doped (101) anatase surface: (**a**) top view and (**b**) side view. Atoms are colored as follows: Ti—light gray, O—red, K—purple, C—medium gray, N—blue, and H—white. Bond distances are shown in Å.

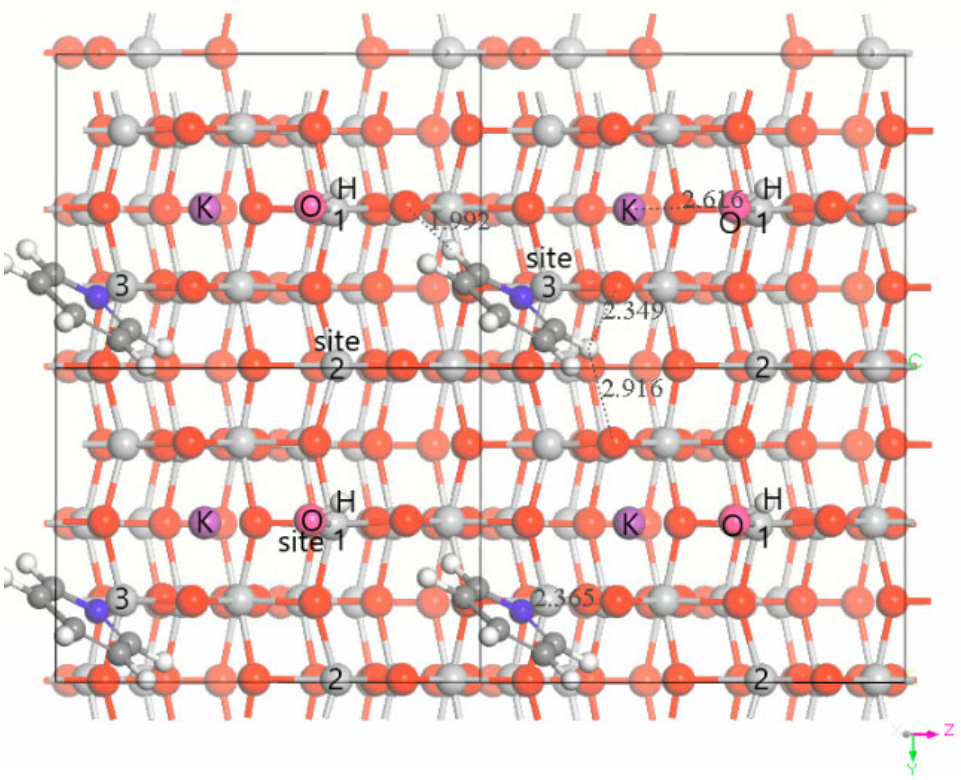

(**a**)

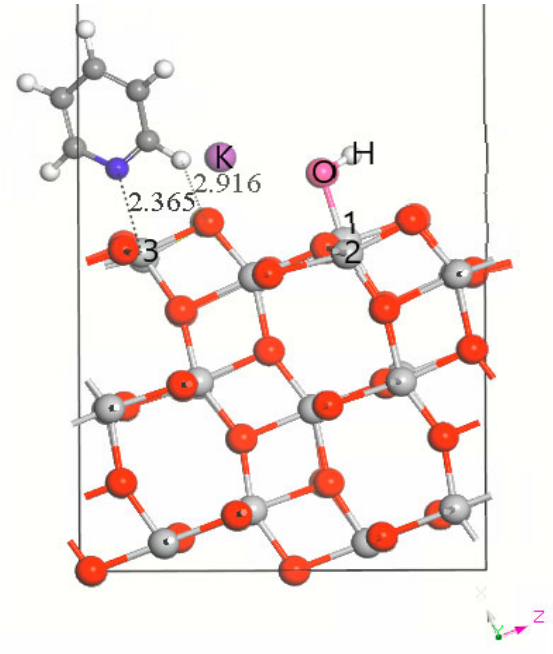

(**b**)

Figure 10. Adsorption of pyridine on site 3 with OH attached to site 1 of KOH-doped (101) anatase surface: (**a**) top view and (**b**) side view. Bond distances are shown in Å.

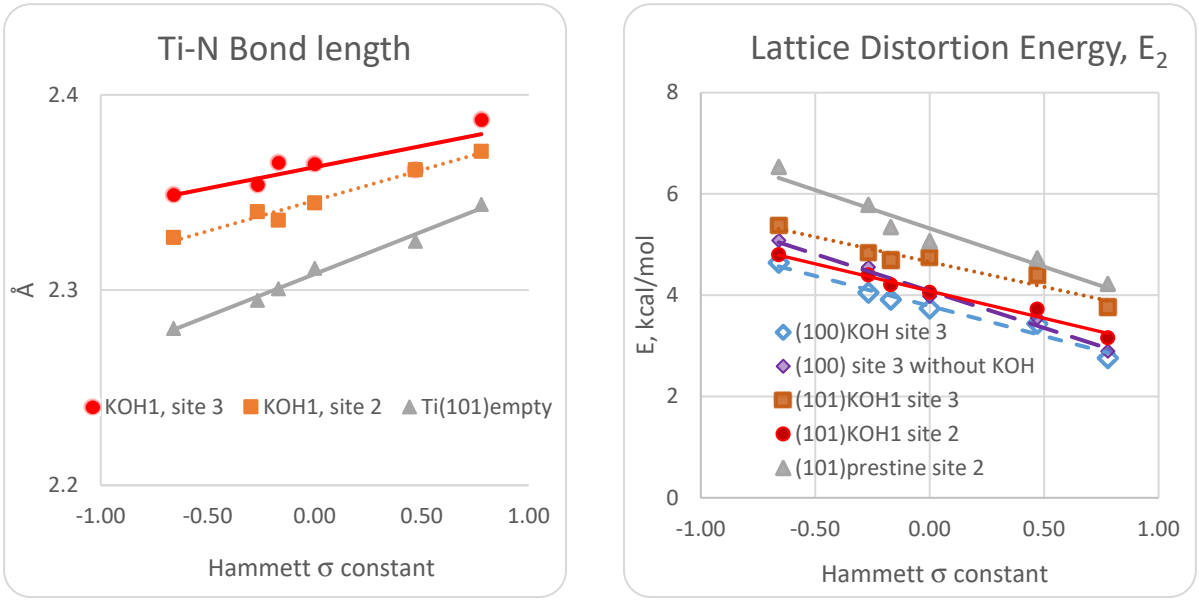

(**a**) (**b**)

Figure 11. Indicators of pyridine interaction with anatase (101) surface depending on the base strength (Hammett σ constant): (**a**) Ti-N bond length and (**b**) lattice distortion energy $\mathbf{E_2}$.

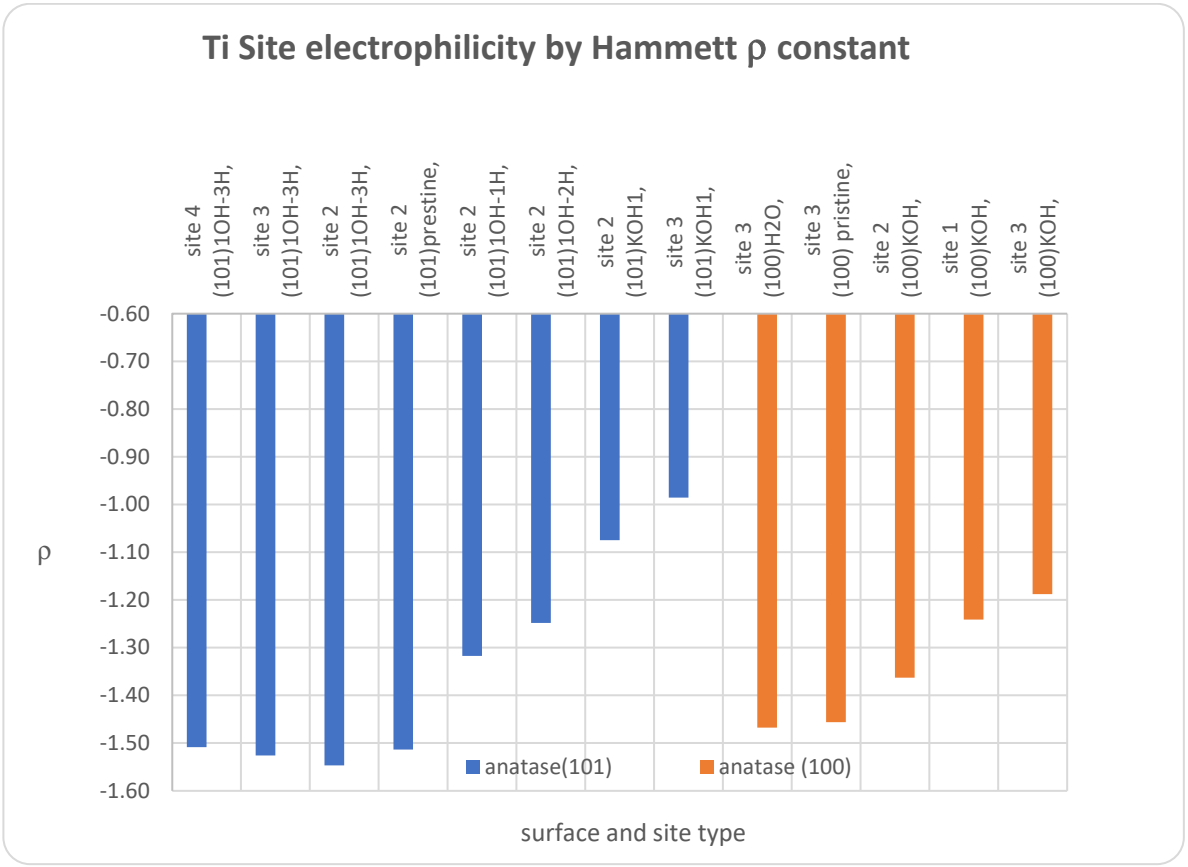

Figure 12. Characterization of acidity (electrophilicity) of different Ti sites on anatase surfaces (100) at 12.5% coverage and (101) at 25% coverage by Hammett ρ constant in presence of dissociated water or KOH, as well as on pristine surfaces.

To evaluate a probing molecule with a weaker basicity, the adsorption of CO was studied on the (101) surface at 25% coverage on the same sites as pyridine, and the effect produced by both adsorbates was compared (Table 1). A smaller lattice distortion energy $\mathbf{E_2}$ is produced by CO adsorption, but there is a good linear correlation at $R^2 = 0.929$ between the use of pyridine and CO as probing molecules for the characterization of surface acidity (Figure S13a). The relation of $\mathbf{E_1}$ energy between two molecules is less linear at $R^2 = 0.707$ (Figure S13b). There is some linear relation between the $\mathbf{E_2}$ energy and the length of C-O and Ti-C bonds observed in agreement with that suggested by Scaranto and Giorgianni [40] as indicators for Lewis acidity of the Ti centers on the anatase (101) surface, along with the IR frequency of CO stretching. Shorter bonds indicate stronger interaction, i.e., stronger Lewis acidity, while IR vibrations shift to a higher frequency.

Table 1. Comparison of $\mathbf{E_1}$–$\mathbf{E_3}$ energies for CO and pyridine adsorption on anatase (101) surface at 25% coverage, kcal/mol, and the length of Ti-C=O bonds.

	CO Adsorption			C=O IR Band, cm^{-1}	C=O Bond Length, Å	Ti-C Bond Length, Å	Pyridine Adsorption		
	E_2	E_1	E_3				E_2	E_1	E_3
K, OH site 1, Adsorbate site 2	0.7	−17.2	−17.9	2184	1.1391	2.5100	4.3	−42.4	−46.7
H site 1, OH site 1, Adsorbate site 2	1.3	−18.2	−19.5	2178	1.1346	2.4912	5.4	−43.5	−48.9
H site 2, OH site 1, Adsorbate site 2	1.7	−19.1	−20.8	2155	1.1346	2.4624	7.7	−46.6	−54.4
H site 3, OH site 1, Adsorbate site 2	1.2	−18.0	−19.2	2171	1.1352	2.4724	5.4	−44.3	−49.6
H site 3, OH site 1, Adsorbate site 3	1.6	−17.7	−19.3	2152	1.1350	2.4661	7.1	−45.1	−52.2
H site 3, OH site 1, Adsorbate site 4	1.0	−16.3	−17.4	2144	1.1362	2.5170	5.5	−42.3	−47.8

3.2. Experimental Study of Pyridine Adsorption in a Pulse Microreactor

The goal of the brief experimental tests was to demonstrate the effect of KOH doping on anatase TiO_2. The amount of adsorbed pyridine found on the surface of anatase samples by the reverse pulse chemisorption method decreased with KOH doping and increasing temperatures (Figure 13). The kinetics of the pyridine exchange for water on the surface followed the first order of the coverage by pyridine. The fitness test shows a straight line of ln(1-A) dependence on the number of pulses, wherein A is the calculated concentration of pyridine in molecules/nm^2 remaining on the surface (Figure S17). The rate constant is in the range of 0.297–0.335 $pulse^{-1}$ at temperatures of 200–350 °C. The half-life is 2.0–2.3 pulses depending on the temperature.

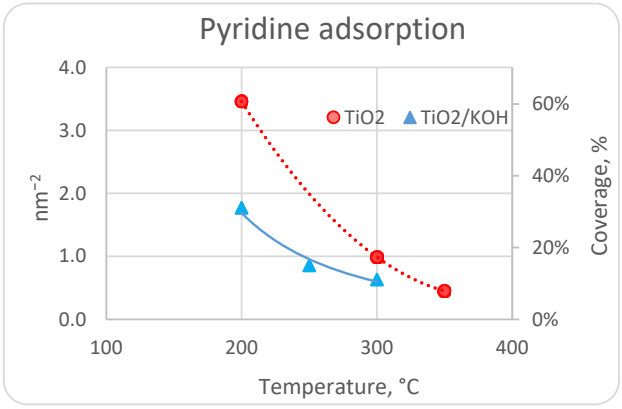

Figure 13. Temperature dependence of pyridine adsorption on anatase TiO_2, undoped (red circles) and doped with KOH (blue triangles), from gas phase, measured by replacement with water in the "inside GC/MS" pulse microreactor.

4. Discussion

The first discussion point is about the choice between using strongly basic pyridine versus weakly basic carbon monoxide. CO minimally perturbs the acidic center structure on the surface, whereas pyridine adsorbs more strongly and disturbs the lattice more. If the goal is to map the surface and measure the relative acidity of surface sites, then either molecule can be used. Both cause similar changes in energy $\mathbf{E_2}$ when moving from one site on a surface to another (Figure S13a), while energy $\mathbf{E_1}$ has a slightly less linear correlation between the two choices (Figure S13b). If a less invasive probing is desired, CO seems to be the right choice. However, even this light molecule causes noticeable lattice distortion, about 20%, on average, of the value produced by pyridine (Table 1). Reagents with comparable basicity, such as carboxylates, in a real catalytic process will likely cause similar changes to the site structure as pyridine. If lattice perturbation is unavoidable, it must be accepted as an integral part of acid–base interactions on surfaces and included in its interpretation.

Pyridine not only interacts with acidic centers by making Ti-N bonds but also by hydrogen bonding between pyridine ortho hydrogen atoms and the lattice oxygen atoms that are basic centers. Variation in the hydrogen-bonding parameters is the likely reason for the less linear correlation between $\mathbf{E_1}$ energies produced by pyridine vs. carbon monoxide adsorption.

The use of various features suggested in the literature for acidity measurement upon the adsorption of probing molecules is validated in the current study for both CO and pyridine interactions with anatase surfaces. Such characteristics as the shrinking of C-O, Ti-C, or Ti-N bonds (Table 1, Figure 11 and Figure S14), the increasing frequency of CO or pyridine ring vibration (Table 1, Figure S18), the rising heat of adsorption, and the growth of lattice distortion energy $\mathbf{E_2}$ (Table S1 and Figure 4, Figure 5, and Figure 7) all point to a stronger acidity of Ti CUS centers. This raises the second point for discussion: is any characteristic better than others, and which one should be used? All are related to the energy of acid–base bond formation, but some may have different levels of quality of fitness because of the differences in the adsorption state. CO has a single point of contact, while pyridine adsorption is complicated by additional hydrogen bonding. On the other hand, the movement of Ti atoms toward the adsorbate (Figure 14) is a universal process surrounding acid–base interactions under various conditions, to which lattice perturbation energy $\mathbf{E_2}$ provides a consistent response. Thus, $\mathbf{E_2}$ has a more linear dependence on the Hammett σ constant of substituents in position 4 of the pyridine ring (Figures 7a and 11b), with high R^2 values, better than those found for $\mathbf{E_1}$ or $\mathbf{E_2}$ energies. For this reason, $\mathbf{E_2}$ energy was chosen to obtain the Hammett rho constant as the measure of the acidity of various centers. Scaranto and Giorgianni have delved even further in their analysis of the non-binding part of the energy changes associated with adsorption and separated lateral interactions into the lattice distortion part and the interaction between adsorbate molecules [22]. The latter becomes negligible at or below 25% coverage, and the lattice distortion energy remains the major or only contributor.

We can now move on to the analysis of factors governing surface acidity. The Hammett rho constant has a negative value that is consistent with the increase in energy of the acid–base interaction upon increasing electron density on the pyridine's nitrogen lone pair by electron-donating substituents. For the same set of pyridine bases, the energy of interaction depends on the strength of the acid. A more negative ρ indicates a stronger acid (Figure 12). For example, the DFT results for the adsorption of pyridines on pristine surfaces find the (101) anatase surface slightly more acidic compared to the (100) surface. In turn, the anatase (101) surface is less acidic than the rutile (110) surface, as also concluded in a DFT study of CO adsorption [22]. Doping anatase surfaces with KOH decreases the acidity of the Ti center, with the effect being more pronounced the closer it is to the potassium atom (Figure 12). These DFT predictions are in good agreement with the experimental results (Section 3.2) that show stronger adsorption of pyridine on undoped anatase TiO_2 samples and weaker adsorption after KOH doping (Figure 13).

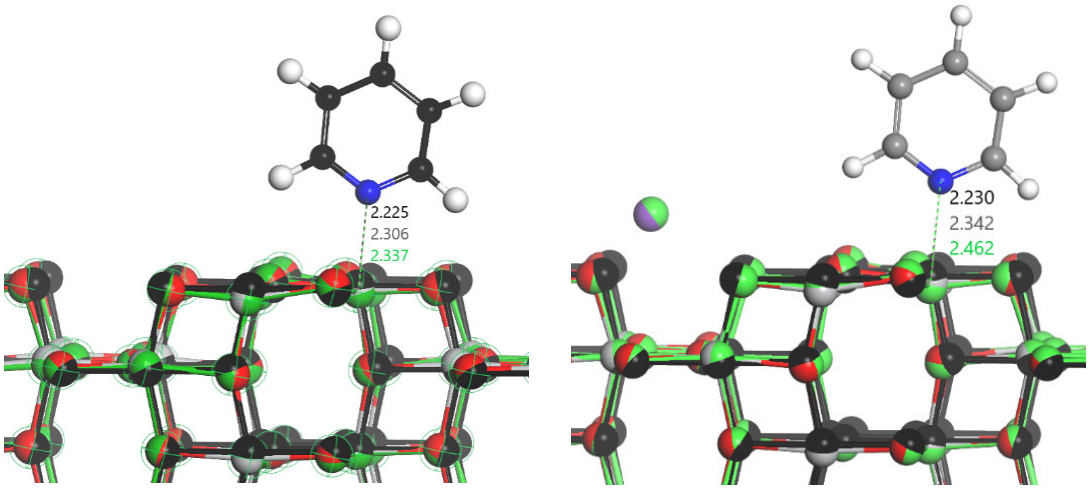

Figure 14. Superimposed structures illustrating the movement of surface top layers upon pyridine adsorption on (100) anatase TiO_2 (**a**) undoped and (**b**) KOH-doped. Bulk positions for lattice atoms are shown in black, cleaved relaxed surface in green, optimized geometry for lattice with adsorbed pyridine in red for oxygen, light gray for titanium, blue for nitrogen, medium gray or black for carbon, and white for hydrogen atoms. Bond distances are shown in Å.

The role of the potassium dopant in the acidity of Ti atoms can be linked to changes in the atomic structure of the surface layer (Figure 14). Upon relaxation of the (100) surface, Ti atoms move inward from their bulk position by 0.112 Å. Electron density moves outward, changing the surface polarization. As a result of pyridine adsorption, the affected Ti atom is pulled back in an outward direction by a small increment of 0.031 Å, remaining 0.081 Å away from reaching the bulk position. On the KOH-doped surface, the inward movement of Ti atoms during the relaxation is even deeper at 0.232 Å, resulting in a higher degree of surface polarization. After pyridine adsorption, the distance remaining for the Ti atom to the bulk position is longer at 0.112 Å. In other words, doping by KOH increases surface polarization by stabilizing the atomic structure of acidic centers. This rigid geometry prevents the Ti atom from coming closer to the pyridine's nitrogen atom and decreases its acidity. The movement of Ti atoms is part of readjusting the surface polarization that is interconnected with the heat of adsorption [24]. It might still be taking place despite overwhelming evidence in recent studies of a significant covalent contribution to bonding in TiO_2 due to the overlapping of titanium d-orbitals with oxygen p-orbitals [41]. At the suggestion of one of the reviewers, it would be interesting for future work to examine metal oxides with a more ionic character, such as MgO and Al_2,O_3, to investigate the presence of the same effect.

Remarkably, when potassium is replaced by a proton, but all other conditions, including the OH position, stay unchanged, the acidity of Ti atoms is significantly increased. This can be attributed to a higher flexibility of lattice oxygen atoms after potassium is removed, passing that flexibility to the titanium atoms. Additionally, it may also happen because of weakening Ti-O bonds in the Ti-O_{2fc}-Ti bridge when its oxygen atom is protonated. Both cases illustrate the change in Lewis acidity because of the surface geometry change induced by KOH or water presence.

5. Conclusions

In this paper, we demonstrate that any characteristics associated with the binding of probing molecules on an anatase titania surface, such as the shrinking of C-O, Ti-C, or Ti-N bonds, the increasing frequency of CO or pyridine ring vibration, the rising heat of adsorption, and the growth of the lattice distortion energy, may be used for the characterization of surface acidity. Contrary to previous beliefs that only weakly binding

molecules should be used to probe surface acidity to avoid interference from lateral effects, we observed a synergy between lattice distortion and acidity so the former can quantify the latter.

The Lewis acidity of anatase titania surfaces is linked to the flexibility of Ti atoms to move toward the adsorbate. When a probing molecule, such as pyridine, acting as a base adsorbs on an anatase titania surface, the titanium atom acid center moves outward from the surface toward pyridine's nitrogen. The more flexible the surface, the more readily the Ti atom is allowed to move, and the acidity of that site measured by the heat of adsorption is stronger.

Alkaline metal dopants stabilize the surface atomic structure making it more rigid and less acidic, while the protonation of Ti-O-Ti bridges increases Ti atoms' flexibility and their Lewis acidity. Due to the lattice distortion being part of the adsorption process, the energy of lattice distortion can be used as a reliable indicator of surface acidity using any specific probing molecules from a broad range of basicities.

Using this method, we were able to classify the anatase (101) surface as more acidic compared to the (100) surface and map the acidity of the doped surfaces. The higher acidity of the surface centers with increasing distance from the alkaline atom is explained by the higher degree of surface flexibility.

Supplementary Materials: The following supporting information can be downloaded at: https://www.mdpi.com/article/10.3390/surfaces7040070/s1, The following file is available free of charge (PDF). Tables S1–S17 include the following: Table S1. Energy for pyridine adsorption on (100) anatase titania surface, Table S2. Bond Distances for pyridine adsorbed on (100) anatase titania surface, Table S3. DFT Calculated energy of substituted pyridines in the gas phase, Table S4. Adsorption of 4-substituted pyridines on Ti5c atom of (100) surface, Table S5. Adsorption of 4-substituted pyridines on site 1 in presence of KOH, Table S6. Adsorption of 4-substituted pyridines on site 2 in presence of KOH, Table S7. Adsorption of 4-substituted pyridines on site 3 in presence of KOH, Table S8. Adsorption of 4-substituted pyridines on site 3 in presence of water, Table S9. Hammett constant for 4-substituted pyridines, Table S10. Adsorption of 4-substituted pyridines on pristine (101) anatase surface, Table S11. Adsorption of 4-substituted pyridines on site 3 of KOH (101) surface, Table S12. Adsorption of 4-substituted pyridines on site 2 of KOH (101) surface, Table S13. Adsorption of 4-substituted pyridines on site 2 of (101) anatase surface in presence of dissociated water with OH on site 1 and H on O2c site 1 (Figure S9a), Table S14. Adsorption of 4-substituted pyridines on site 2 of (101) anatase surface in presence of dissociated water with OH on site 1 and H on O2c site 2 (Figure S9b), Table S15. Adsorption of 4-substituted pyridines on site 2 of (101) anatase surface in presence of dissociated water with OH on site 1 and H on O2c site 3 (Figure S9c), Table S16. Adsorption of 4-substituted pyridines on site 4 of (101) anatase surface in presence of dissociated water with OH on site 1 and H on O2c site 3 (Figure S10a), Table S17. Adsorption of 4-substituted pyridines on site 3 of (101) anatase surface in presence of dissociated water with OH on site 1 and H on O2c site 3 (Figure S10b), Table S18. Adsorption of 4-substituted pyridines through nitrogen protonation by the OH group of KOH doped (101) anatase surface (Figure S11a). Figures S1–S18 include total energies, bond energies, lattice distortion energies, bond lengths, energy correlations between pyridine and CO adsorption, maps of adsorption sites, atomic scale models of surfaces with adsorbates, Hammett plots, GC/MS calibration of pyridine and water mixtures, fitness test for the first order kinetics, and IR vibration frequency. Reference [42] are cited in the Supplementary Materials.

Author Contributions: The manuscript was written through the contributions of all authors. All authors have given approval to the final version of the manuscript. A.V.I. designed the computations and experiments and prepared the manuscript for the publication. P.E.D. ran the DFT computations and GCMS experiments and collected and prepared data. All authors have read and agreed to the published version of the manuscript.

Funding: This work is supported directly by the National Science Foundation under research grant No. 1955130.

Data Availability Statement: The data supporting the findings of this study are included within the manuscript.

Acknowledgments: Support from the National Science Foundation and St. John Fisher University for this work is greatly acknowledged. A.V.I. thanks the Chemistry Department at SJFC for its continuous support.

Conflicts of Interest: The authors declare no conflict of interest.

Abbreviations

DFT, density functional theory; GCMS, gas chromatography–mass spectrometry; TPD, temperature programmed desorption; BET, Brunauer–Emmett–Teller.

References

1. Tsang, C.H.A.; Li, K.; Zeng, Y.; Zhao, W.; Zhang, T.; Zhan, Y.; Xie, R.; Leung, D.Y.C.; Huang, H. Titanium Oxide Based Photocatalytic Materials Development and Their Role of in the Air Pollutants Degradation: Overview and Forecast. *Environ. Int.* **2019**, *125*, 200–228. [CrossRef] [PubMed]
2. Khaleel, A. Titanium-Doped Alumina for Catalytic Dehydration of Methanol to Dimethyl Ether at Relatively Low Temperatures. *Fuel* **2011**, *90*, 2422–2427. [CrossRef]
3. Ignatchenko, A.V. Multiscale Approach for the Optimization of Ketones Production from Carboxylic Acids by the Decarboxylative Ketonization Reaction. *Catal. Today* **2019**, *338*, 3–17. [CrossRef]
4. Parida, K.; Mishra, H.K. Catalytic Ketonisation of Acetic Acid over Modified Zirconia. *J. Mol. Catal. A Chem.* **1999**, *139*, 73–80. [CrossRef]
5. Ignatchenko, A.V.; King, M.M. Catalyst for the Production of Methyl Isopropyl Ketone. U.S. Patent 7,501,379, 10 March 2009.
6. Beavers, W.A.; Ignatchenko, A.V.; Liu, Z.; Ashcroft, C.D.; White, T.M. Catalyst and Process for the Preparation of Unsymmetrical Ketones. U.S. Patent 2007/0100166, 3 May 2007.
7. Pham, T.N.; Sooknoi, T.; Crossley, S.P.; Resasco, D.E. Ketonization of Carboxylic Acids: Mechanisms, Catalysts, and Implications for Biomass Conversion. *ACS Catal.* **2013**, *3*, 2456–2473. [CrossRef]
8. Ignatchenko, A.V.; DeRaddo, J.S.; Marino, V.J.; Mercado, A. Cross-Selectivity in the Catalytic Ketonization of Carboxylic Acids. *Appl. Catal. A Gen.* **2015**, *498*, 10–24. [CrossRef]
9. Ignatchenko, A.V.; Springer, M.E.; Walker, J.D.; Brennessel, W.W. Alkyl Substituted Beta-Keto Acids: Molecular Structure and Decarboxylation Kinetics in Aqueous Solution and on the Surface of Metal Oxides. *J. Phys. Chem. C* **2021**, *125*, 3368–3384. [CrossRef]
10. Marie, O.; Ignatchenko, A.V.; Renz, M. Methyl Ketones from Carboxylic Acids as Valuable Target Molecules in the Biorefinery. *Catal. Today* **2020**, *367*, 258–267. [CrossRef]
11. Ignatchenko, A.V.; Diprospero, T.J.; Patel, H.; Lapenna, J.R. Equilibrium in the Catalytic Condensation of Carboxylic Acids with Methyl Ketones to 1,3-Diketones and the Origin of the Reketonization Effect. *ACS Omega* **2019**, *4*, 11032–11043. [CrossRef]
12. Ding, S.; Wang, H.; Han, J.; Zhu, X.; Ge, Q. Ketonization of Propionic Acid to 3-Pentanone over $Ce_xZr_{1-x}O_2$ Catalysts: The Importance of Acid-Base Balance. *Ind. Eng. Chem. Res.* **2018**, *57*, 17086–17096. [CrossRef]
13. Boekaerts, B.; Sels, B.F. Catalytic Advancements in Carboxylic Acid Ketonization and Its Perspectives on Biomass Valorisation. *Appl. Catal. B* **2021**, *283*, 119607. [CrossRef]
14. Ignatchenko, A.V. Density Functional Theory Study of Carboxylic Acids Adsorption and Enolization on Monoclinic Zirconia Surfaces. *J. Phys. Chem. C* **2011**, *115*, 16012–16018. [CrossRef]
15. Wang, S.; Iglesia, E. Experimental and Theoretical Evidence for the Reactivity of Bound Intermediates in Ketonization of Carboxylic Acids and Consequences of Acid–Base Properties of Oxide Catalysts. *J. Phys. Chem. C* **2017**, *121*, 18030–18046. [CrossRef]
16. Pulido, A.; Oliver-Tomas, B.; Renz, M.; Boronat, M.; Corma, A. Ketonic Decarboxylation Reaction Mechanism: A Combined Experimental and DFT Study. *ChemSusChem* **2013**, *6*, 141–151. [CrossRef] [PubMed]
17. Ignatchenko, A.V.; McSally, J.P.; Bishop, M.D.; Zweigle, J. Ab Initio Study of the Mechanism of Carboxylic Acids Cross-Ketonization on Monoclinic Zirconia via Condensation to Beta-Keto Acids Followed by Decarboxylation. *Mol. Catal.* **2017**, *441*, 35–62. [CrossRef]
18. Zecchina, A.; Lamberti, C.; Bordiga, S. Surface Acidity and Basicity: General Concepts. *Catal. Today* **1998**, *41*, 169–177. [CrossRef]
19. Mekki-Berrada, A.; Auroux, A. Thermal Methods. In *Characterization of Solid Materials and Heterogeneous Catalysts: From Structure to Surface Reactivity*; Che, M., Vedrine, J.C., Eds.; Wiley-VCH: Paris, France, 2012; Volume 1, pp. 777–782.
20. Strunk, J.; Bañares, M.A.; Wachs, I.E. Vibrational Spectroscopy of Oxide Overlayers. *Top. Catal.* **2017**, *60*, 1577–1617. [CrossRef]
21. Halawy, S.A.; Osman, A.I.; Abdelkader, A.; Nasr, M.; Rooney, D.W. Assessment of Lewis-Acidic Surface Sites Using Tetrahydrofuran as a Suitable and Smart Probe Molecule. *ChemistryOpen* **2022**, *11*, e202200021. [CrossRef]
22. Scaranto, J.; Giorgianni, S. A Quantum-Mechanical Study of CO Adsorbed on TiO_2: A Comparison of the Lewis Acidity of the Rutile (110) and the Anatase (101) Surfaces. *J. Mol. Struct. THEOCHEM* **2008**, *858*, 72–76. [CrossRef]
23. Plata, J.; Collico, V.; Márquez, A.; Fdez Sanz, J. Analysis of the Origin of Lateral Interactions in the Adsorption of Small Organic Molecules on Oxide Surfaces. *Theor. Chem. Acc.* **2012**, *132*, 1311. [CrossRef]

24. Guermeur, R.; Jacolin, C. Influence of Surface Silanols on the Dielectric Properties of Nitrogen Adsorbed on Activated Silica. *Surf. Sci.* **1994**, *315*, 323–336. [CrossRef]
25. González-Torres, J.C.; Cipriano, L.A.; Poulain, E.; Domínguez-Soria, V.; García-Cruz, R.; Olvera-Neria, O. Optical Properties of Anatase TiO_2: Synergy between Transition Metal Doping and Oxygen Vacancies. *J. Mol. Model.* **2018**, *24*, 276. [CrossRef]
26. Verma, P.; Truhlar, D.G. Does DFT+U Mimic Hybrid Density Functionals? *Theor. Chem. Acc.* **2016**, *135*, 182. [CrossRef]
27. Long, R.; English, N.J. Electronic Properties of Anatase-TiO_2 Codoped by Cation-Pairs from Hybrid Density Functional Theory Calculations. *Chem. Phys. Lett.* **2011**, *513*, 218–223. [CrossRef]
28. Ignatchenko, A.V.; Kozliak, E.I. Distinguishing Enolic and Carbonyl Components in the Mechanism of Carboxylic Acid Ketonization on Monoclinic Zirconia. *ACS Catal.* **2012**, *2*, 1555–1562. [CrossRef]
29. Ignatchenko, A.; Hill, J.; Gray, J.; Nealon, D.; Dushane, R. Innovative Use of a Gas Chromatograph for Heterogeneous Catalytic Studies. In Proceedings of the 18th NACS Meeting, Cancun, Mexico, 1–6 June 2003; Volume 7444, p. 169. Available online: https://www.nacatsoc.org/18nam/Posters/P169-Innovative%20use%20of%20a%20Gas%20Chromatograph%20for%20heterogeneo.pdf (accessed on 5 November 2024).
30. Ignatchenko, A.V.; Nealon, D.G.; Dushane, R.; Humphries, K. Interaction of Water with Titania and Zirconia Surfaces. *J. Mol. Catal. A Chem.* **2006**, *256*, 57–74. [CrossRef]
31. Wang, S.; Iglesia, E. Experimental and Theoretical Assessment of the Mechanism and Site Requirements for Ketonization of Carboxylic Acids on Oxides. *J. Catal.* **2017**, *345*, 183–206. [CrossRef]
32. Delley, B. An All-Electron Numerical Method for Solving the Local Density Functional for Polyatomic Molecules. *J. Phys. Chem.* **1990**, *92*, 508–517. [CrossRef]
33. Delley, B. From Molecules to Solids with the DMol3 Approach. *J. Chem. Phys.* **2000**, *113*, 7756–7764. [CrossRef]
34. Burdett, J.K.; Hughbanks, T.; Miller, G.J.; Richardson, J.W.; Smith, J.V. Structural-Electronic Relationships in Inorganic Solids: Powder Neutron Diffraction Studies of the Rutile and Anatase Polymorphs of Titanium Dioxide at 15 and 295 K. *J. Am. Chem. Soc.* **1987**, *109*, 3639–3646. [CrossRef]
35. Perdew, J.P.; Burke, K.; Ernzerhof, M. Generalized Gradient Approximation Made Simple. *Phys. Rev. Lett.* **1996**, *77*, 3865–3868. [CrossRef] [PubMed]
36. Tkatchenko, A.; Scheffler, M. Accurate Molecular Van Der Waals Interactions from Ground-State Electron Density and Free-Atom Reference Data. *Phys. Rev. Lett.* **2009**, *102*, 73005. [CrossRef] [PubMed]
37. Clark, S.J.; Segall, M.D.; Pickard, C.J.; Hasnip, P.J.; Probert, M.J.; Refson, K.; Payne, M.C. First Principles Methods Using CASTEP. *Z. Für Krist.* **2005**, *220*, 567–570. [CrossRef]
38. Krukau, A.V.; Vydrov, O.A.; Izmaylov, A.F.; Scuseria, G.E. Influence of the Exchange Screening Parameter on the Performance of Screened Hybrid Functionals. *J. Chem. Phys.* **2006**, *125*, 224106. [CrossRef]
39. Ambrosetti, A.; Reilly, A.M.; DiStasio, R.A., Jr.; Tkatchenko, A. Long-Range Correlation Energy Calculated from Coupled Atomic Response Functions. *J. Chem. Phys.* **2014**, *140*, 18A508. [CrossRef] [PubMed]
40. Scaranto, J.; Giorgianni, S. DFT Calculations of Carbon Monoxide Adsorbed on Anatase TiO_2 (101) and (001) Surfaces: Correlation between the Binding Energy and the CO Stretching Frequency. *Mol. Simul.* **2013**, *39*, 245–249. [CrossRef]
41. Koch, D.; Manzhos, S. On the Charge State of Titanium in Titanium Dioxide. *J. Phys. Chem. Lett.* **2017**, *8*, 1593–1598. [CrossRef] [PubMed]
42. Hammett, L.P. The Effect of Structure upon the Reactions of Organic Compounds. Benzene Derivatives. *J. Am. Chem. Soc.* **1937**, *59*, 96–103. [CrossRef]